INSTITUTE OF PHYSICS PUBLISHING JOURNAL OF MICROMECHANICS AND MICROENGINEERING

J. Micromech. Microeng. **16** (2006) 620–630 doi:10.1088/0960-1317/16/3/018

Modeling and characterization of a carbon fiber emitter for electrospray ionization

A K Sen[1], J Darabi[1], D R Knapp[2] and J Liu[2]

[1] MEMS and Microsystems Laboratory, Department of Mechanical Engineering, University of South Carolina, 300 Main Street, Columbia, SC 29208, USA
[2] Department of Pharmacology, Medical University of South Carolina, 173 Ashley Avenue, Charleston, SC 29425, USA

E-mail: darabi@engr.sc.edu

Received 26 October 2005, in final form 11 December 2005
Published 16 February 2006
Online at stacks.iop.org/JMM/16/620

Abstract

A novel microscale emitter employing a pointed carbon fiber (CF) can be used for electrospraying in mass spectrometric (MS) analysis. The carbon fiber is located coaxial with a fused silica capillary tube of 360 μm OD and 75 μm ID with its sharp tip extending 30 μm beyond the tube terminus. The electrospray ionization (ESI) process is simulated using a computational fluid dynamics (CFD) code based on the Taylor–Melcher leaky-dielectric fluid model for solving the electrohydrodynamics and the volume of fluid (VOF) approach for tracking the liquid–gas interface. The CFD code is first validated for a conventional geometry and then used to simulate the CF emitter based ESI model. The simulated current–flow and current–voltage results are in good agreement with experimental results for the CF emitter. The effects of emitter geometry, potential difference, flow rate and the physical properties of the liquid on the electrospray behavior of the CF emitter are thoroughly investigated. The spray current and jet diameter are correlated with the flow rate, potential difference and physical properties of the liquid and the correlation results are quantitatively compared with the results reported in the literature.

(Some figures in this article are in colour only in the electronic version)

1. Introduction

There has been tremendous growth in MS analysis in terms of sensitivity, speed and level of structural information since the late 1980s with implementation of two ionization techniques: matrix assisted laser desorption ionization (MALDI) and electrospray ionization (ESI). Until the early 1980s, electron impact (EI) or chemical ionization (CI) methods were used for ionizing small biomolecules which are amenable to gas chromatography. But large, thermally sensitive, non-volatile samples cannot be analyzed by EI or CI-MS techniques without suitable prior treatment [1]. The ESI technique enables analysis of such large molecules directly from the liquid phase [2]. Zeleny [3, 4] demonstrated that a liquid solution can be sprayed from a capillary by applying a high electric potential across its exit. The pioneering work of Dole [5, 6] and Fenn [7] has indicated ESI as an ionization method for large compounds such as polymers and biomolecules. Followed by these, the processes and mechanisms involved in the gas-phase ion generation by this technique have been widely investigated. In the ESI method, gaseous ionized molecules are produced from a liquid solution by generating a fine spray of droplets in the presence of a strong electric field. This ability of the ESI process has found its natural application in the study of proteins and other biomolecules. Various processes involved in the ESI method are presented in figure 1.

The ESI potential is commonly applied to the sample liquid externally through the emitter tube coated with conductive materials, but it can also be applied internal to

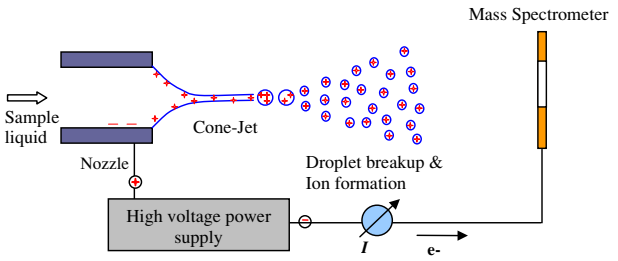

Figure 1. Schematic of an ESI process.

the liquid sample. Herring and Qin [8] have shown an ESI interface for capillary electrophoresis (CE) in which the electrospray potential is applied through a palladium wire inserted into the emitter tip. In Chiou's design [9], the high voltage for the electrospray was applied through the built-in electrode integrated with a sample reservoir, a microchannel and a silica capillary nozzle in a small PDMS chip. Cao and Moini [10] designed an electrospray emitter in which the ESI voltage was applied via an electrode placed inside a capillary tube and the electrical contact was maintained through a small hole in the capillary wall near its exit. Electrospraying is possible at lower voltages using emitters with smaller capillary diameters ($\sim$10 μm), but the smaller apertures can clog easily due to excessive back pressure. It is easier to handle emitters with larger diameters (>50 μm). But they are not as efficient as the smaller diameter emitters [11].

As a common practice, for applying ESI voltage, a conductive coating is applied on the outer periphery of the low flow emitters fabricated from insulating materials such as glass or fused silica. It has been observed that the sputter-coated noble metal layer on the tip of a fused silica capillary deteriorates quickly affecting its durability. The quick deterioration of the coating can be due to the electrical discharge, electrochemical reactions and poor mechanical bonding between the layer and the fused-silica surface. The lifetime of such emitters can be increased by electroplating of gold following sputter coating [12] or by coating SiO_x over the sputter-coated gold [13]. Gold-coated emitters on top of adhesion layers of chromium or nickel alloy can provide excellent bonding and are durable when operating as cathodes. But while operating as anodes, the adhesion layers are chemically dissolved through the gold film. Alternative conductive coatings have been evaluated to improve the stability and durability of the emitters. A colloidal graphite-coated emitter was used for stable ESI operation and has shown a long-term life time [14]. The polyaniline (PANI)-coated emitters have shown high durability and are resistant to electrical discharge, because of the thick coatings. A comparison of electrospray ionization behavior of PANI-coated and gold-coated nanospray emitters showed that PANI-coated emitters provide similar enhanced sensitivity that gold-coated emitters exhibit [15]. Graphite–polyimide mixture has also been used as conductive coating in case of seathless electrospray emitters. The stability of the conductive coating has been investigated by electrochemical methods which revealed good performances during oxidative stress [16]. Capability of a carbon-coated emitter was demonstrated for micro-spray and sheathless CE and ESI applications. Though this emitter was not rugged, it was durable enough for seathless CE or ESI applications [17].

We have introduced a novel ESI emitter based on a pointed carbon fiber that can eliminate the clogging problem and avoid the contact problem between sample liquid and gold layer thereby enhancing the applicability, reliability and durability of the ESI system [18]. In this work, the carbon fiber-based ESI emitter is simulated using a computational fluid dynamics (CFD) software package FLOW3D [19]. Experiments are performed using the new CF emitter. The model predictions are compared with experimental results. The ESI performance of the novel emitter is evaluated by studying its response to various parameters such as geometry of the emitter, flow rate, physical properties of the liquid, which affect the electrospray process. Spray current and jet diameter are correlated with flow rate and the properties of the liquid and the correlation results are quantitatively compared with the results reported in the literature.

In the following section, the theory of electrohydrodynamics governing the ESI process is described with reference to the Taylor–Melcher leaky-dielectric fluid model [20]. Then validation of the CFD code is presented by considering the ESI configuration used by Hartman *et al* [21]. Furthermore, simulation and experimental results for the CF-based ESI model are presented and discussed. Finally, results of the parametric study and the correlations are presented and discussed.

2. Theory

The cone-jet phase of the ESI process can be explained under the purview of Navier–Stoke's equations governing the fluid motion and Maxwell's equations controlling the electromagnetic phenomena. Consider any physical system (liquid) in the laboratory in which an electric field $\vec{E}$ is present. If the liquid obeys Ohm's law and magnetic field is determined by the free charge current density, the magnetic field intensity ($\vec{B}$) can be expressed as $\vec{B} \sim \sigma\mu\vec{E}\ell$, where σ is the electrical conductivity, μ is the permeability and ℓ is the characteristic length of the system. The ratio of electrical energy to magnetic energy for such a system is $\vec{E}/c\vec{B} \sim 1/\sigma^*$, where $c = \sqrt{1/\varepsilon\mu}$ is the speed of light in the system and ε is the permittivity of the sample liquid, σ^* is a dimensionless number equal in numerical value to the conductivity of the liquid in SI units. Therefore, for leaky-dielectric fluids characterized by very low values of electrical conductivity, magnetic forces are negligible and Maxwell's equations are reduced to the electroquasistatic limit, falling in the realm of electrohydrodynamics (EHD) [22].

The CFD code is based on the Taylor–Melcher leaky-dielectric fluid model [20] and involves two different fluids: leaky-dielectric fluid (liquid sample) and air (ESI medium). In the present model, the bulk-free charge density in the liquid is assumed to be zero and the electric field $\vec{E}$ is irrotational and divergence-free throughout the field. However, due to conduction, charges are carried out to the fluid–air interface where coupling between fluid and the electric field occurs. In the case of perfect conductors or dielectric fluids, the electric stress is normal to the interface and changes in the interface profile along with surface tension force balance

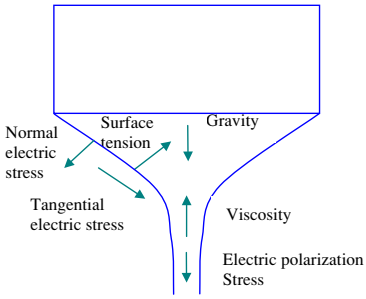

Figure 2. Forces in the liquid cone.

the electric stress. In the case of leaky-dielectric fluids, the interfacial charges modify the electric field and viscous flow is developed to balance the force developed due to the tangential components of the field acting on the interface. The various kinds of stresses acting on the Taylor cone are indicated in figure 2.

To summarize, the governing equation for the electric field in the bulk fluid and at the interface is

$$\nabla^2\phi = 0. \tag{1}$$

At the fluid–air interface, the tangential component of the electric field $\vec{E} = -\nabla\phi$ is continuous, but there is a jump of the electric field in the normal direction, which is proportional to the surface charge density q,

$$\vec{n}\cdot(\varepsilon_l\nabla\phi_l - \varepsilon_m\nabla\phi_m) = q \tag{2}$$

$$\vec{t}_i\cdot(\varepsilon_l\nabla\phi_l - \varepsilon_m\nabla\phi_m) = 0, \tag{3}$$

where ϕ is the electric potential, $\vec{n}$ is the unit normal of the interface directed in to the ESI medium, $\vec{t}_i$ represents either of two orthogonal tangent vectors embedded in the surface. ε_l and ε_m are permittivities of liquid and the medium, respectively. The accumulation of interfacial charge density q is represented by the charge conservation equation,

$$\frac{\mathrm{d}q}{\mathrm{d}t} = -\vec{n}\cdot\sigma(\nabla\phi_l), \tag{4}$$

where $\mathrm{d}/\mathrm{d}t$ is the Lagrangian derivative and σ is the electrical conductivity of the liquid. The free charges accumulated at the interface induce an electric field normal to its surface which results in normal (T_n) and tangential (T_t) stresses acting on the interface,

$$T_n = \tfrac{1}{2}[\varepsilon_l(\vec{n}\cdot\nabla\phi_l)^2 - \varepsilon_m(\vec{n}\cdot\nabla\phi_m)^2] \tag{5}$$

$$T_t = -q(\vec{t}_i\cdot\nabla\phi). \tag{6}$$

Assuming the liquid to be incompressible (of constant density ρ) and of constant viscosity η, its motion can be described by the continuity and momentum conservation equations,

$$\nabla\cdot\vec{u} = 0 \tag{7}$$

$$\rho\frac{\mathrm{d}\vec{u}}{\mathrm{d}t} = -\nabla p + \eta\nabla^2\vec{u} + \vec{f}_e + \rho\vec{g}, \tag{8}$$

where $\vec{u}$ is the flow velocity, p is the fluid pressure and $\vec{f}_e$ is the electromechanical force. The expression for the electromechanical force can be derived from thermodynamic considerations [23],

$$\vec{f}_e = \nabla\cdot\vec{T}^e = \rho_e\vec{E} - \tfrac{1}{2}|\vec{E}|^2\nabla\varepsilon + \nabla p_{st}, \tag{9}$$

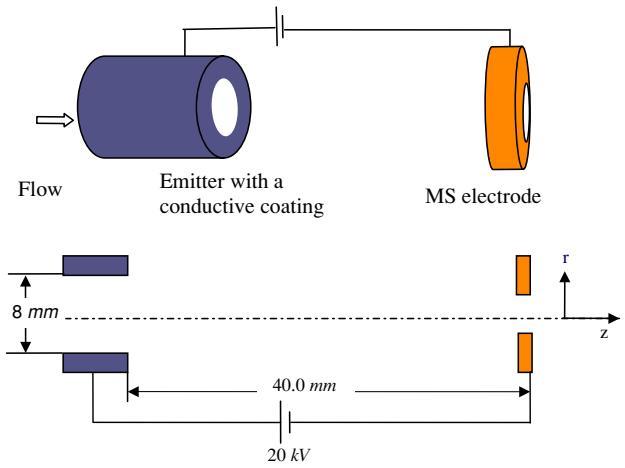

Figure 3. Schematic of the ESI model studied by Hartman *et al* [21].

where $\vec{T}^e$ is the electrical stress tensor, ρ_e is the net free charge density and $p_{st} = \frac{1}{2}(\varepsilon - \varepsilon_o)|\vec{E}|^2$ is known as the electrostrictive pressure. Where ε and ε_0 are the permittivity of the liquid and vacuum, respectively. The first term in equation (9), known as the Coulomb force, is the strongest EHD force and is the force per unit volume on a medium containing free electric charge. The second term, called the dielectrophoretic force, arises due to the force exerted by an electric field on a non-homogeneous dielectric fluid. The third term represents the electromechanical force density due to the non-uniformity of the electric field.

The tracking of the free surface is achieved using the volume of fluid (VOF) technique [24]. In the VOF method, the motion of the interface between the liquid and air is defined by a volume fraction function F, and the interface is tracked by the following conditions:

$$F(x,y,z,t) = \begin{cases} 0 & \text{outside the liquid} \\ 1 & \text{inside the liquid} \\ >0, <1 & \text{on the free surface.} \end{cases} \tag{10}$$

The volume fraction function F is governed by the volume fraction equation,

$$\frac{\mathrm{d}F}{\mathrm{d}t} + \vec{u}\cdot\nabla F = 0, \tag{11}$$

which represents the kinematic condition at the interface.

3. Validation

The electrode configuration tested by Hartman *et al* [21] is shown in figure 3. A potential difference of 20 kV was maintained between the capillary nozzle of 8 mm diameter and the counter electrode for electrospraying ethylene glycol with the following physical properties: density $\rho = 1109\ \mathrm{kg\,m^{-3}}$, coefficient of viscosity $\mu = 0.02$ Pa s, coefficient of surface tension $\gamma = 0.048\ \mathrm{Nm^{-1}}$, dielectric constant $k = 37$ and electrical conductivity $\sigma = 72\ \mu\mathrm{Sm^{-1}}$. The counter electrode was located at a distance of 40 mm from the nozzle. The liquid flow rate was maintained at $1.4 \times 10^{-9}\ \mathrm{m^3\ s^{-1}}$ because the experimental results were available at this flow rate.

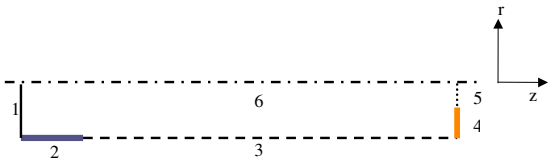

Figure 4. Boundaries of the computational domain for the validation model.

3.1. Boundary conditions

In the FLOW3D code [19], the Navier–Stokes equations for the flow in the liquid, Laplace equations for the electric potentials in the liquid and outside, and the conservation equation for the free charge density on the interface are solved. The boundary conditions for the above model are described with reference to figure 4. Boundary 1 (inflow boundary): uniform velocity $\vec{u}_z = u_0$, stagnation pressure, fluid fraction function $F = 1$, where $u_0 = Q/A$, A is the flow cross-sectional area of the nozzle and Q is the flow rate. Boundary 2: no slip boundary conditions $\vec{u}_r = \vec{u}_z = 0$, where $\vec{u}_r$ and $\vec{u}_z$ are radial and axial velocity components, respectively, electric potential $\phi = \phi_0$, where ϕ_0 is the applied potential difference. Boundary 3 and 6: symmetric boundary conditions, $\frac{\partial \phi}{\partial r} = 0$, $\vec{u}_r = 0$, $\frac{\partial \vec{u}_z}{\partial r} = 0$. Boundary 4: $\phi = 0$. Boundary 5: continuative boundary conditions, $\frac{\partial \phi}{\partial z} = 0$, $\frac{\partial \vec{u}_z}{\partial z} = 0$, $F = 0$. The boundary conditions at the liquid–gas interface involve balance of surface tension, pressure, viscous stresses and electric stresses (equation (5) and (6)) and electrostatic conditions. The electrical boundary conditions on the interface consider that the tangential components of the electric field $\vec{E}$ are continuous (equation (3)) and the normal components jump by an amount proportional to the free charge density q (equation 2). The kinematic condition at the interface is presented in equation (11). The mechanical boundary condition at the interface is governed by

$$\vec{n} \cdot [\vec{T}^m + \vec{T}^e] \cdot \vec{n} = \gamma \nabla \cdot \vec{n}, \tag{12}$$

where $\vec{T}^m$ is the mechanical stress tensor, γ is the coefficient of surface tension. In the formulation of Maxwell's electromechanical stress tensor, the pressure, which is negative of average of normal stresses, contains an electromechanical component in addition to the hydrodynamic component. To build a fully coupled electrohydrodynamic formulation, in addition to adding a source term (K–H force density) to the momentum equation, the pressure boundary conditions need to be modified to incorporate the electromechanical pressure component. This code is based on a well-established multiphase flows hydrodynamics code [24]. The gradient of electromechanical pressure is included as an additional component of the electromechanical force density preserving the pressure itself as purely hydrodynamic. Thus, the EHD coupling is achieved through an additional source term in the momentum equation alone, eliminating the necessity to modify the existing pressure-related boundary conditions. Additionally, the interface around the lip of the nozzle exit is maintained by assigning a contact angle that represents the force due to surface tension and the cosine of that angle. The initial conditions for the liquid are: $\vec{u}_z = u_0$, $q = 0$ and the fluid fraction function on the interface $F = 0.5$.

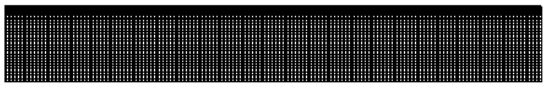

Figure 5. Non-uniform meshing with 300 axial cells and 30 radial cells.

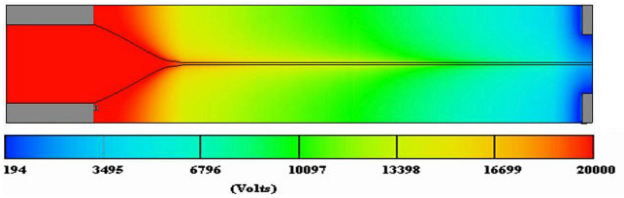

Figure 6. Cone-Jet profile and the electric potential contours at 19 kV; cone length is 4.3 mm.

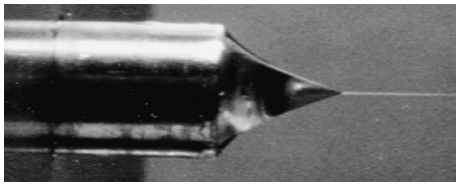

Figure 7. A photograph of the experimental cone shape; cone length is 4.2 ± 0.2 mm [21].

3.2. Results and discussion

Figure 5 shows an axisymmetric (about z-axis) computational mesh build around the model, with 300 axial cells and 30 radial cells. The shape of the simulated cone-jet along with the electric potential contours is presented in figure 6. The image of the cone-jet obtained through experiments is shown in figure 7, in which case the liquid conductivity was measured to be 73 μSm^{-1}. The size of a cone-jet can be specified by the cone length, which is defined as the distance between the nozzle tip and the position on the cone where the jet emerges. At a potential difference of 20 kV, the length of the simulated cone is 3.9 mm, which matches well with the measured cone length of 4.2 ± 0.2 mm.

The variation of ESI current as a function of liquid flow rate for a mixture of ethylene glycol and LiCl with electrical conductivity of 72 μSm^{-1} and 186 μSm^{-1} is plotted in figure 8. The electrospray current (I) was calculated using the following relation [21]:

$$I = I_{\text{cond}} + I_{\text{conv}} = \pi R_s^2 \vec{E}_z \sigma + 2\pi R_s \vec{u}_z q, \tag{13}$$

where I_{cond} and I_{conv} are the conduction and convection current, respectively, R_s is the jet radius, $\vec{E}_z$ is the electric field on the surface of the jet along the z-direction, $\vec{u}_z$ is the velocity of jet in the z-direction and q is the surface charge density. The ESI current obtained in the simulation was approximately 8–10% higher than the experimental values for the mixture of ethylene and LiCl with a conductivity of 72 μSm^{-1} and approximately 5% higher when the conductivity is 186 μSm^{-1}.

A possible explanation for the underestimation of cone length and deviation in the current-flow characteristics is the neglect of space charge. The presence of the charged droplets reduces the electric field around the cone-jet compared to the situation where they are neglected. It has been shown that for

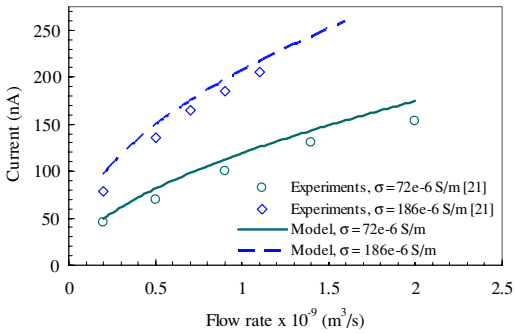

Figure 8. ESI current as a function of flow rate as predicted by the model and previous experiments.

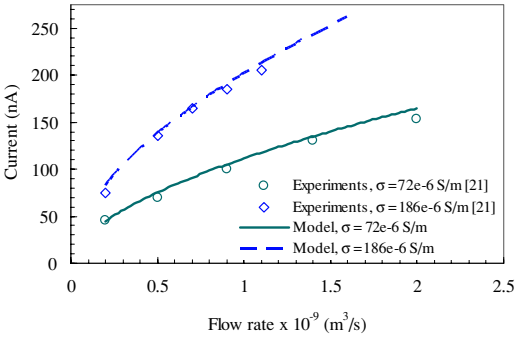

Figure 9. ESI current as a function of flow rate by considering the effect of space charge.

Table 1. Current-flow characteristics for the validation model.

Liquid	σ (μS m^{-1})	n_{IQ} experiments [21]	n_{IQ} model
Ethylene glycol 99% + LiCl	72	0.492	0.495
Ethylene glycol 99% + LiCl	186	0.479	0.482

the present electrode configurations the effect of space charges can be taken into account by reducing the potential difference by 5–7% [21]. When the effect of space charge is considered, the length of the simulated cone predicted by the model was computed to be 4.3 mm which is approximately the same as the experimental value. Figure 9 shows a comparison of current-flow characteristics obtained from the simulation at 19 kV and experiments at 20 kV. The results indicate an excellent agreement between the model predictions and experimental results.

The current-flow characteristics for the validation model are fitted using the following relation:

$$I = m_{IQ} Q^{n_{IQ}}, \tag{14}$$

where m_{IQ} and n_{IQ} are constants, whose values are presented in table 1. The value of n_{IQ} calculated from the model corresponds to the case where the influence of space charge is included. As shown in table 1, the agreement between the experimental results and model prediction is within 1%. In addition, the values of constant n_{IQ} is consistent with the observations of many researchers which show that the electric current I is proportional to the square root of the flow rate, $Q^{1/2}$ [25–28].

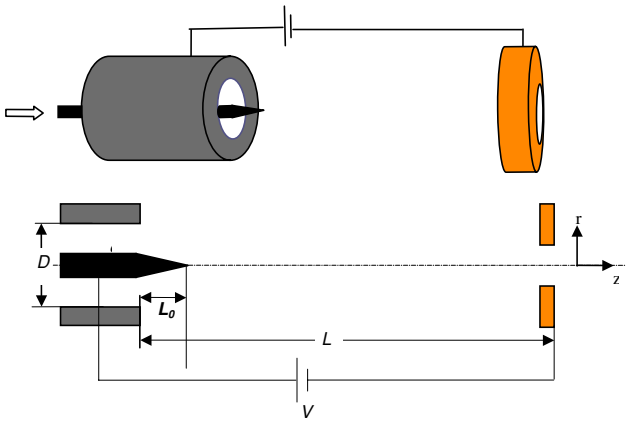

Figure 10. Configuration of the CF-based ESI model.

4. CF emitter-based ESI model

A schematic diagram of the carbon fiber-based ESI model is shown in figure 10. The emitter consists of a pointed carbon fiber of diameter d located coaxial with a fused silica capillary tube of diameter D. The pointed tip of the carbon fiber extends beyond the tube terminus by a length L_o. A constant potential difference of V_o is applied between the carbon fiber and the counter electrode which is located at a distance L from the capillary tube terminus. The elctrospray is produced by infusing a leaky-dielectric fluid of density ρ, viscosity μ, electrical conductivity σ, dielectric constant k, and surface tension coefficient γ at a constant volumetric flow rate Q.

4.1. Boundary conditions

The boundary conditions for the CF-based model are similar to the BCs described in section 3.1 with the exception that in this case the potential is applied on the carbon fiber instead of the capillary tube surface. The fused silica capillary tube is modeled as an insulated material with a dielectric constant of 3.9.

4.2. Results and discussions

The geometry of the ESI model considered in the present simulation is as follows: $D = 75$ μm, $d = 30$ μm, $L_o = 30$ μm. The counter electrode is located at a distance of 0.4 mm from the nozzle ($L = 0.4$ mm). A potential difference of 900 V was maintained between the carbon fiber and the counter electrode for electrospraying a mixture of MeOH/H2O/HOAc with the following physical properties: density $\rho = 1030$ kg m^{-3}, coefficient of viscosity $\mu = 0.008$ Pa s, coefficient of surface tension $\gamma = 0.037$ N m^{-1}, dielectric constant $k = 55$ and electrical conductivity $\sigma = 135$ μS m^{-1}. The liquid flow rate is maintained at 300 nL min^{-1}.

Figure 11 shows an axisymmetric (about z-axis) computational mesh built around the model with 300 axial cells and 50 radial cells. The maximum electric field intensity as a function of total number of cells in the computational domain is shown in figure 12. The mesh near the axis of symmetry was refined along the radial direction to capture

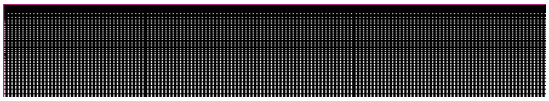

Figure 11. Non-uniform meshing for the CF-based ESI model, 300 axial cells and 50 radial cells.

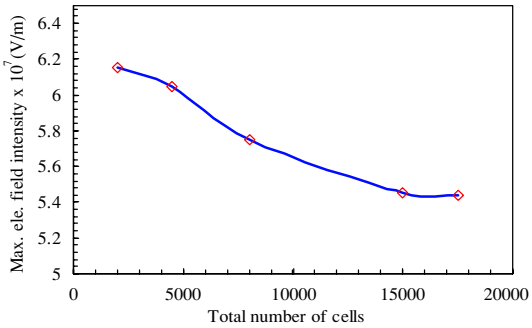

Figure 12. Maximum electric field intensity versus total number of cells in the computational domain.

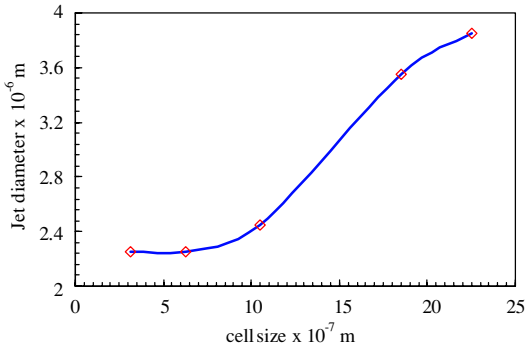

Figure 13. Jet diameter versus cell size in the radial direction, measured 50 μm away from the tube terminus.

the thin jet. Figure 13 indicates that the cells near the jetting region were small enough and a good resolution was achieved with cell size less than 0.7 μm in the radial direction. The jet diameter is defined at a section of the jet where it does not vary along the z-direction which was approximately 50 μm away from the tube terminus.

Figure 14 shows time evolution of the free surface of the cone-jet along with the electric potential contours in the computational domain. When the apex of the Taylor cone profile reaches the tip of the carbon fiber, a jet evolves and remains steady with time. Attainment of a steady-state solution was ensured by observing no change in the potential distribution, electric field intensity, charge density, and velocity with time. A relative residue of 1.0×10^{-7} was specified in all simulations. In this particular case, the steady state was reached at time 8.0×10^{-3} s. The Taylor cone was always confined to the sharp tip of the carbon fiber once the steady state was reached. The electric field intensity contours are presented in figure 15. The results depict a large jump in the electric field across the free surface of the cone-jet profile, which is responsible for the normal and tangential electric stresses. The normal stress maintains the cone shape and the tangential stress accelerates the liquid towards the jet. The

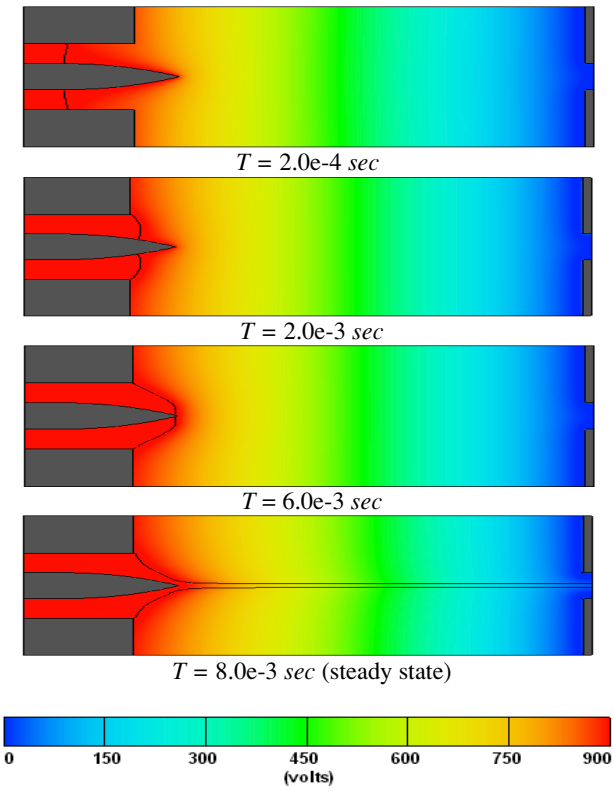

Figure 14. Cone-jet profiles and the electric potential contours at various time steps.

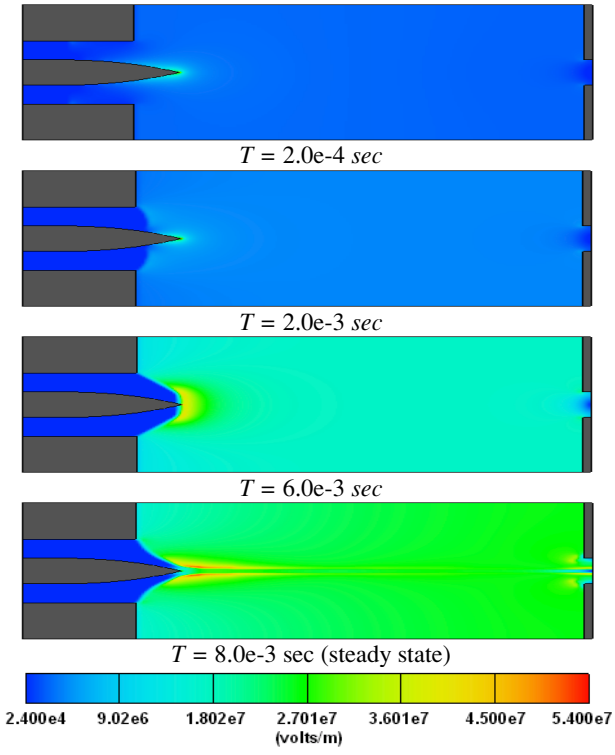

Figure 15. Electric field contours at various time steps.

jet velocity along the axial direction is presented in figure 16. As seen there, the liquid is accelerated as it moves along the z-direction due to action of tangential stresses. The variation

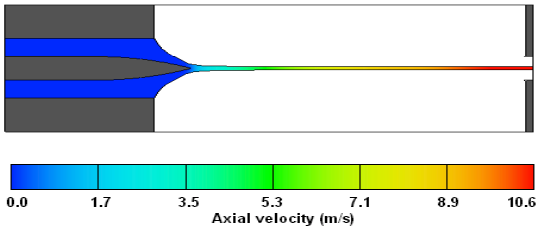

Figure 16. Axial jet velocity contours at steady state ($T = 10.0$ e–3 s).

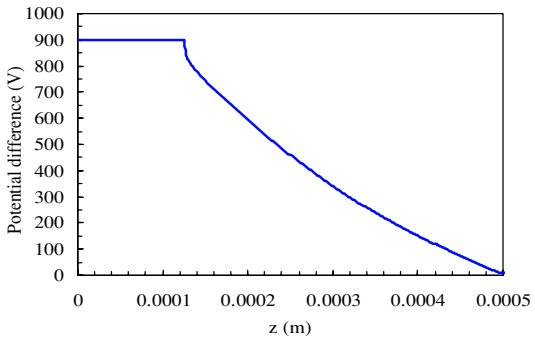

Figure 17. Variation in the electric potential along the cone-jet axis ($T = 2$ e–4 s).

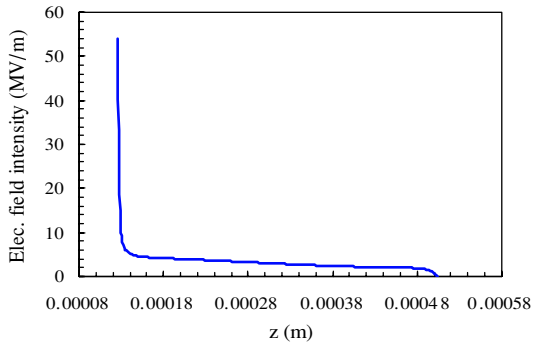

Figure 18. Variation in electric field intensity along the cone-jet axis ($T = 2.0$ e–4 s).

in the electric potential and electric field along the cone-jet axis is presented in figures 17 and 18, respectively. There is a large drop in the electric potential near the tip of the carbon fiber which results in a strong electric field at this region. The charge density contours on the cone-jet are shown in figure 19. As expected, the free charges are mainly accumulated near the interfacial region conforming to the leaky-dielectric model. Some charges are induced on the inner periphery of the insulated capillary.

4.3. Experimental results

The ESI system used for testing had a capillary diameter of the emitter of 75 μm and diameter of the carbon fiber of 30 μm. The tip of the carbon fiber extended 30 μm beyond the emitter tube terminus. The liquid was MeOH/H2O/HOAc (48:48:4 by volume). A ThermoFinnigan (San Jose, CA) LCQ classic ion trap mass spectrometer was used for applying the electric potential. The counter electrode (8 mm OD and flat

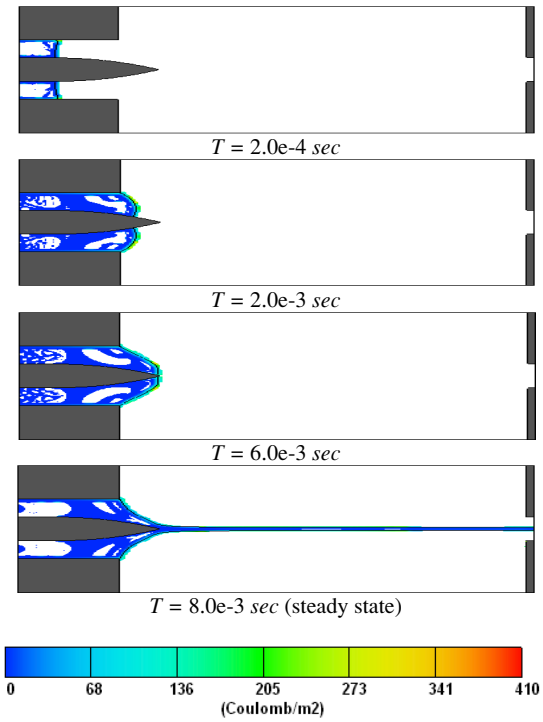

Figure 19. Electric charge density contours at various time steps.

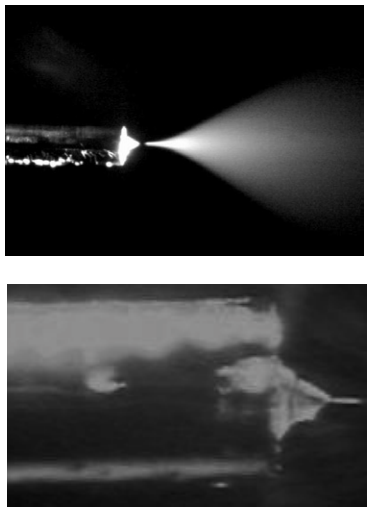

Figure 20. Top: image of electrospray, bottom: cone-jet profile using the CF emitter. Distance between the carbon fiber tip and the counter electrode is 4.0 mm, potential difference is 3500 V, flow rate is 300 nL min^{-1}.

end) was the standard sampling capillary of LCQ. The flow rate was set by a LCQ equipped software controlled syringe pump (Hamilton 50 μm glass syringe). The spray current data were read as the readings shown in the voltage-monitoring window equipped with LCQ control software. The image of the ESI process was captured using a Panasonic CCD camera (WV-BP332) attached via a 9.5 mm extension tube to a 4X microscope objective. More details regarding the experimental setup can be found in [18].

The experimental results of the ESI process are shown in figure 20. The top image shows the electrospray plume

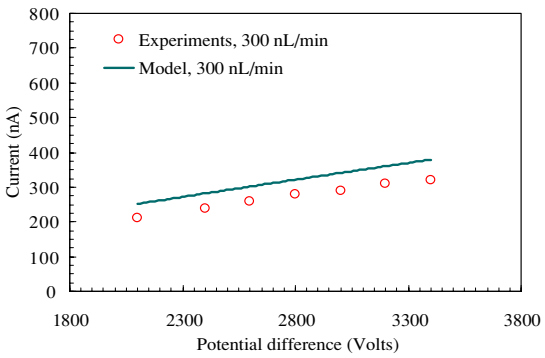

Figure 21. Spray current as a function of potential difference. The distance between the CF tip and the counter electrode is 4.0 mm.

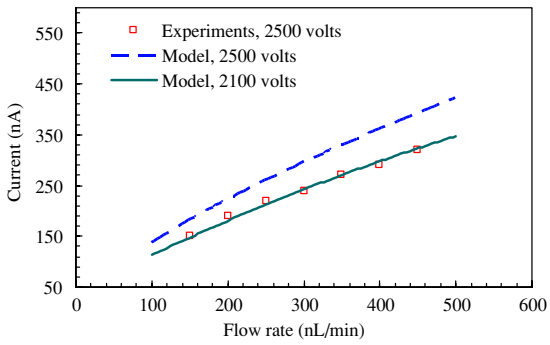

Figure 22. Spray current as a function of flow rate. The distance between the CF tip and the counter electrode is 4.0 mm.

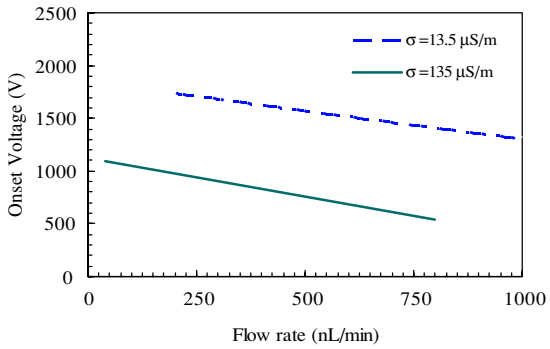

Figure 23. Variation of onset potential with flow rate for different electrical conductivities.

generated and the bottom one shows a close-up view of the cone-jet profile. There is a good qualitative match between the shapes of the Taylor cones predicted by the model and the experiment. In both cases the length of the Taylor cone is limited by the tip of the carbon fiber and the base of the cone is attached to the inner periphery of the capillary. The lengths of the jet predicted in the simulation and observed in the experiments are different. This is because the present model simulates the cone-jet phase of the ESI process and it is not intended to simulate the jet break-up or columbic explosion regimes of the ESI process. Thus, the length of the jet extends from the apex of the cone to the counter electrode satisfying conservation of mass. In reality, a jet exits the cone and breaks down into primary and secondary droplets because of electrical instabilities.

The current–voltage characteristics predicted by the model and the experiments are presented in figure 21. It can be observed that the value of the current measured in the experiment is lower than the values predicted by the model which may be due to neglect of space charge. However, as discussed earlier the effect of space charge on the cone-jet dynamics is considered by lowering the potential difference by a certain percentage. It was found that the current value measured in the experiment at 2800 V is the same as the current value predicted by the model at 2400 V. This indicates that the effect of space charge on the potential difference is around 15%.

The spray current and voltage are correlated via the following relation:

$$I = m_{IV} V^{n_{IV}}. \tag{15}$$

The value of n_{IV} is found to be 0.86 for the measured data. The increase in spray current with increase in the electric potential has been reported by Ganan-Calvo *et al* [29]. The value of the exponent n_{IV} was predicted to be 0.4–0.7 by Hartman *et al* [21]. In the same work, they showed that the electrode diameter had an impact on the current–voltage characteristics. The value of n_{IV} found in the case of CF emitter is higher, which may be because of its micro-scale configuration. The minimum size of the capillary nozzle selected by Hartman *et al* [21] had a diameter of 1.0 mm which is much larger than the diameter of the CF emitter (75 μm) in the present work.

The current-flow characteristics measured in the experiments and predicted by the model are shown in figure 22.

The model matches well with the experimental results when the value of potential difference is reduced by 15%. The spray current measured from experiments and predicted by the model are correlated with flow rate according to equation (14). The value of the constant n_{IQ} predicted from our model is 0.575 which matches well with the value of 0.583 as measured from our experiments. The value of n_{IQ} for the model is calculated by including the effect of space charge. The value of n_{IQ} is found to be within 15% of the reported value of 0.5 in the literature [25–27].

4.4. Parametric study

The CF emitter is parameterized based on onset potential, spray current, jet diameter, physical properties of the liquid and geometry of the emitter. The effect of space charge is accounted by reducing the potential difference by 15%.

The minimum electric potential required to generate a stable cone-jet is termed as 'onset potential'. The variation of onset potential with flow rate is presented in figure 23. A lower value of onset potential is preferred as it makes handling of the ESI system much easier. Low flow emitters are beneficial in terms of low sample consumption. An appropriate flow rate and the associated onset potential have to be used based on the sample availability and operating conditions. It is observed that the onset potential for a less conductive liquid is higher. Similar behavior has been reported by Cloupeau *et al* [30] based on experimental results.

A higher value of ESI current is expected to yield enhancement of the ion production process. The increase

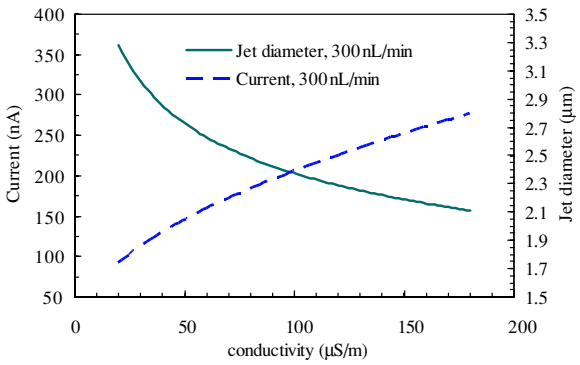

Figure 24. Variation of spray current and jet diameter with conductivity at a potential difference of 1045 V.

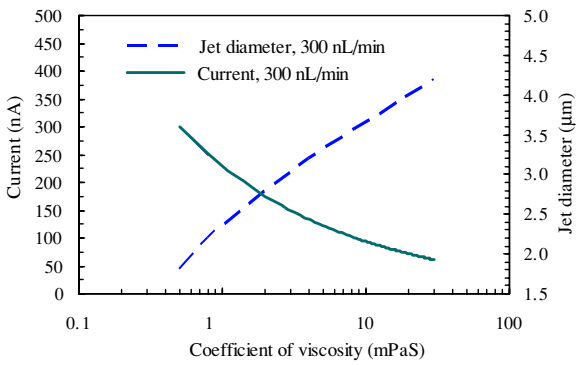

Figure 26. Variation of ESI current and jet diameter with viscosity at a potential difference of 1045 V.

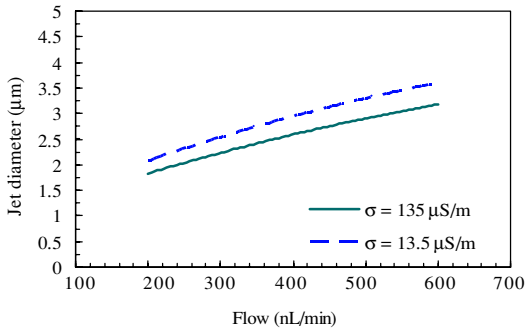

Figure 25. Variation of jet diameter with flow rate for different conductivities at a potential difference of 1045 V.

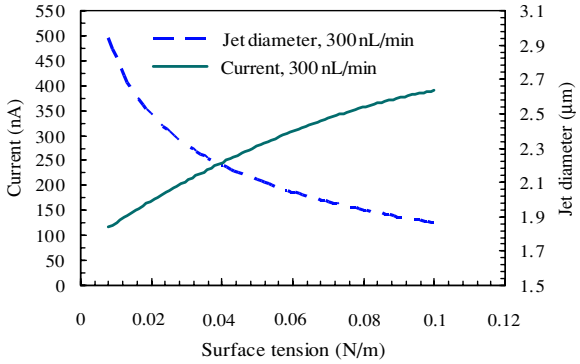

Figure 27. Variation of ESI current and jet diameter with surface tension at a potential difference of 1045 V.

in spray current and decrease in jet diameter with increase in conductivity is shown in figure 24. The spray current and jet diameter are correlated with conductivity as follows:

$$I = m_{I\sigma}\sigma^{n_{I\sigma}} \tag{16}$$

$$d = m_{d\sigma}\sigma^{n_{d\sigma}}. \tag{17}$$

The value of the constant $n_{I\sigma}$ is calculated to be 0.522 which is close to the value of 0.5 reported by Ganan-Calvo [26] and Fernandez de la Mora [25]. The constant $n_{d\sigma}$ is determined to be –0.185 which is reported to be $-1/6$ by Ganan-Calvo [26] and $-1/3$ by Fernandez de la Mora [25].

Figure 25 shows variation of jet diameter with flow rate. The jet diameter d increases with increase in flow rate and the correlation is fitted as follows:

$$d = m_{dQ}Q^{n_{dQ}}. \tag{18}$$

The constant n_{dQ} is determined to have a value equal to 0.546 which matches well with a value of 0.5 predicted by Ganan-Calvo [26], but deviates from $1/3$ predicted by Fernandez de la Mora [25]. Also, it is observed that at a fixed flow rate the jet diameter is higher for a less conductive liquid.

Variation of ESI current and jet diameter with viscosity is depicted in figure 26. The results indicate a decrease in spray current and an increase in jet diameter with increase in viscosity. The spray current and jet diameter can be correlated with viscosity through the following relations:

$$I = m_{I\mu}\mu^{n_{I\mu}} \tag{19}$$

$$d = a_{d\mu}\ln(\mu) + b_{d\mu}. \tag{20}$$

The value of the constant $n_{I\mu}$ was calculated to be –0.388. Previous experiments [21] have shown that spray current decreases with increase in viscosity. The relation between jet diameter and viscosity is found to be logarithmic. The value of constants is calculated to be $a_{d\mu} = 0.578$ and $b_{d\mu} = 2.31$.

Figure 27 depicts the variation of ESI current and jet diameter with surface tension. The results indicate that the spray current increases and jet diameter decreases with increase in surface tension. The spray current and jet diameter are correlated with surface tension as follows:

$$I = m_{I\gamma}\gamma^{n_{I\gamma}} \tag{21}$$

$$d = m_{d\gamma}\gamma^{n_{d\gamma}}. \tag{22}$$

The constant $n_{I\gamma}$ has a value equal to 0.531 which is in agreement with a value of 0.5 reported by Ganan-Calvo [26] and Fernandez de la Mora [25]. The constant $n_{d\gamma}$ is determined to be –0.183, which was reported to be $-1/6$ by Ganan-Calvo [26].

The need for a higher onset potential for a liquid with higher surface tension is indicated by figure 28. For a fixed value of surface tension, an emitter with smaller capillary diameter requires lower onset potential. This is because reduction in the capillary diameter results in an increase in the strength of the electric field. Hence, micro- and nano-emitters with smaller capillary diameters are superior for electrospraying of high aqueous content fluids, characterized

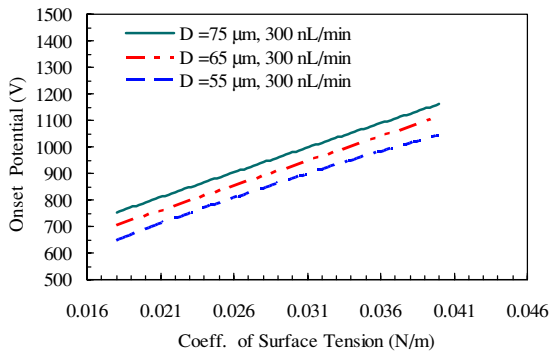

Figure 28. Variation of onset potential with coefficient of surface tension for different capillary diameters.

by higher surface tension. However, a clogging issue may arise if the diameter is too small.

5. Conclusion

A novel microscale emitter employing a pointed carbon fiber suitable for MS analysis is presented. The CF emitter-based ESI model is simulated using a computational fluid dynamics code. The novel emitter is observed to generate a stable cone-jet for a wide range of flow rates, applied potential and liquid properties, thus making it suitable for MS analysis. It is observed that the apex of the Taylor cone was always confined to the sharp tip of the carbon fiber where the electric field is the highest and the base of the Taylor cone is always limited to the inner periphery of the capillary. Experiments were performed using the CF emitter to capture the image of the cone-jet and measure current-flow and current–voltage characteristics. A good agreement between the model predictions and experimental results is obtained when the effect of space charge is considered. It is found that for electrospraying high aqueous content liquid, capillaries of smaller diameters can be used in order to limit the onset potential. The electrospray current and jet diameter are correlated with flow rate, potential difference and liquid properties such as conductivity, viscosity and surface tension. The correlation results are in agreement with the results reported in the literature.

Acknowledgments

This work was supported in part by a grant from the University of South Carolina Research and Productive Scholarship Fund, NIH-NCI grant CA86285 and the NIH-NHLBI Proteomics Initiative via contract N01-HV-28181.

References

[1] Siuzdak M 1996 *Mass Spectrometry for Biotechnology* (New York: Academic)
[2] Cole R B (ed) 1997 *Electrospray Ionization Mass Spectrometry* (New York: Wiley-Interscience)
[3] Zeleny J 1914 *Phys. Rev.* **3** 69–91
[4] Zeleny J 1917 *Phys. Rev.* **10** 1–6
[5] Dole M, Mack L L, Hines R L, Mobley R C, Ferguson L D and Alice M B 1968 Molecular beams of macroions *J. Chem. Phys.* **49** 2240–9
[6] Clegg G A and Dole M 1971 Molecular beams of macroions: III. Zein and polyvinylpyrrolidone *Biopolymers* **10** 821–6
[7] Fenn J B, Mann M, Meng C K, Wong S F and Whitehouse C M 1989 Electrospray ionization for mass spectrometry of large biomolecules *Science* **246** 64–71
[8] Herring C J and Qin J 1999 An on-line preconcentrator and the evaluation of electrospray interfaces for the capillary electrophoresis/mass spectrometry of peptides *Rapid Commun. Mass Spectr.* **13** 1–7
[9] Chiou C H, Lee G B, Hsu H T, Chen P W and Liao P C B 2002 Microscale Tools for Sample Preparation, Separation and Detection of Neuropeptides *Sensors Actuators* B **86** 280–6
[10] Cao P and Moini M 1997 A novel sheathless interface for capillary electrophoresis/electrospray ionization mass spectrometry using an in-capillary electrode *J. Am. Soc. Mass Spectrom* **8** 561–4
[11] Janini G M, Conards T P, Wilkens K L, Issaq H J and Veenstra T D 2003 A sheathless nanoflow electrospray interface for on-line capillary electrophoresis mass spectrometry *Anal. Chem* **75** 1615–9
[12] Barroso M B de Jong and Ad P 1999 Sheathless preconcentration-capillary zone electrophoresis-mass spectrometry applied to peptide analysis *J. Am. Soc. Mass Spectrom* **10** 1271–8
[13] Valaskovic G A and McLafferty F W 1996 Long-lived metallized tips for nanoliter electrospray mass spectrometry *J. Am. Soc. Mass Spectrom.* **7** 1270–2
[14] Zhu X, Thiam S, Valle B C and Warner I M 2002 A colloidal graphite coated emitter for seathless capillary electrophoresis/nanoelectrospray ionization mass spectrometry *Anal. Chem* **74** 5405–9
[15] Maziarz E P I II, Lorenz S A, White T P and Wood T D 2000 Polyaniline: a conductive polymer coating for durable nanospray emitters *J. Am. Soc. Mass. Spectrom* **11** 659–63
[16] Nilsson S, Wetterhall M, Bergquist J, Nyholm L and Markides K E 2001 A simple and robust conductive graphite coating for sheathless electrospray emitters used in capillary electrophoresis/mass spectrometry *Rapid Commun. Mass Spectr.* **15** 1997–2000
[17] Chang Y Z and Her G R 2000 Sheathless capillary electrophoresis/electospray mass spectrometry using a carbon-coated tapered fused silica capillary with a beveled edge *Anal. Chem.* **72** 626–30
[18] Liu J, Ro K W, Busman M and Knapp D R 2004 Electrospray ionization with a pointed carbon fiber emitter *Anal. Chem.* **76** 3599–606
[19] Hirt C W 2004 Electro-hydrodynamics of semi–conductive fluids: with application to electro–spraying *Flow Science Technical Note 70* FSI–04–TN70 1–7
[20] Saville D A 1997 Electrohydrodynamcis: the Taylor–Melcher leaky dielectric model *Annu. Rev. Fluid Mech.* **29** 27–64
[21] Hartman R P A, Brunner D J, Camelot D M A, Marijnissen J C M and Scarlett B 1999 Electrohydrodynamic atomization in the cone-jet mode physical modeling of the liquid cone and jet *J. Aerosol Sci.* **30** 823–49
[22] Castellanos A 1998 Basic Concepts and Equations in Electrohydrodynamics *Electrohydrodynamics* ed A Castellanos (Berlin: Springer)
[23] Melcher J R 1981 *Continuum Electromechanics* (Cambridge, MA: MIT Press)
[24] Hirt C W and Nichols B D 1981 Volume of fluid (VOF) method for the dynamics of free boundaries *J. Comp. Phys.* **39** 201–25
[25] De la Mora F J and Loscertales I G 1994 The current emitted by highly conducting Taylor cones *J. Fluid Mech.* **260** 155–84

[26] Ganan-Calvo A M 1997 Cone–jet analytical extension of Taylor's electrostatic solution and the asymptotic universal scaling laws in electrospraying *Phys. Rev. Lett.* **79** 217–20
[27] Higuera F J 2004 Current/flow–rate characteristic of an electrospray with a small meniscus *J. Fluid Mech.* **513** 239–46
[28] Zeng J, Sobek D and Korsmeyer T Electro-hydrodynamic modeling of electrospray ionization: cad for a microfluidic device-mass spectrometer interface *Transducers '03: 12th Int. Conf. on Solid State Sensors, Actuators and Microsystems* **2** 1275–8
[29] Ganan–Calvo A M, Davila J and Barrero A 1997 Current and droplet size in the electrospraying of liquids. Scaling laws *J. Aerosol Sci.* **28** 249–75
[30] Cloupeau M and Prunet-Foch B 1989 Electrostatic spraying of liquids in cone–jet mode *J. Electrost.* **22** 135–59